Synthesis of $SnO-Sb_2O_5$ ceramic anodes coated with cadmium and calcium ferrites for the depletion of emerging contaminants

J. Mora-Gómez[1], M. García-Gabaldón[1], S. Mestre[2], V. Pérez-Herranz[1], D. M. García-García[1], J. Carrillo-Abad[3]

1) IEC Group, Universitat Politècnica de València, Camí de Vera s/n, 46022, València, Spain

2) University Institute of Ceramic Technology, Chemical Engineering Department, Universitat Jaume I, Castellón, Spain

3) CALAGUA – Unitat Mixta UV-UPV, Department D'Enginyeria Química, Universitat de València, Avinguda de La Universitat s/n, Burjassot, València, 46100, Spain

Corresponding author: jumogme@upvnet.upv.es

Abstract

This manuscript studies cadmium and calcium ferrite coatings on a ceramic electrode, based on tin oxide doped with antimony, to be used as photoanodes in the degradation of atenolol, as a model emerging contaminant. Solution combustion synthesis and thermal treatment were used to generate and fix ferrite precursors over the electrode surface, respectively. Firstly, the physical and photoelectrochemical characterization of these ceramic ferrites was carried out. Photoluminescence measurements indicated an emission band between the orange-red zone of the visible spectrum and the near infrared, which the basic ceramic electrode did not show. Furthermore, an improvement in the photocatalytic activity of ferrites was observed by linear sweep voltammetry and light pulsed chronoamperometry tests. The band gap energies obtained were 1.3 and 2.64 eV for cadmium and calcium ferrites, respectively. Subsequently, both ferrites were tested in photoelectrooxidation assays using atenolol. The

degradation of the contaminant was greater under light irradiation conditions than in the darkness for both anodes. Increasing the applied current density enhanced both atenolol degradation and mineralization but worsened the mineralization current efficiency and energy consumed per gram of total organic carbon removed. Comparing the type of electrode, cadmium ferrite showed better results as a photoanode than calcium ferrite in terms of degradation and mineralization of the atenolol.

Keywords

Ceramic electrode, Electrochemical property, Ferrite, Photo-electrochemistry

1. Introduction

Heterogeneous photocatalysis has been under extensive study from their discovery in the 1972 by Fujishima et al. [1]. It appeared as a promising technology for environmental purification [2] and clean and renewable energy generation [3]. Sunlight is a renewable source of clean energy, and is the preferred choice as a reagent for photocatalysis due to its abundance, free-cost, and environmentally friendly nature [4].

Although the use of titanium dioxide (TiO_2) and its composites presents several advantages [5], their main drawback is its inherent wide band gap (3.2 eV), so it is only photoactive in UV light. This means that these kind of photocatalysts only make use of 4% of the solar spectrum [6,7]. Therefore, the use of efficient solar light harvesting systems is a more economical and straightforward solution that

has directed the scientists' interests to the research of visible light-absorbing semiconductors [4,8,9].

Some metal oxides (MOs) are promising light absorbers because of their stability in water, abundance, low cost and biocompatibility [10–13]. Ferrites (iron-containing mixed oxides) are one of the most abundant minerals that inherit most of the properties of hematite, as they are sunlight absorbers due to their narrow bandgap (≈ 2 eV) [9], but they are much less studied. Ferrites may crystallize as ABO_3 and AB_2O_4 stoichiometries, where A and B are metallic cations, being iron (III) the main species, with perovskite or the most common spinel type structures. The later ferrites have two different crystallographic sites, tetrahedral and octahedral (A and B sites) coordinated to oxygen atoms [10,14].

Spinel ferrites have become promising materials due to their narrow bandgap (1.1-2.3 eV), low toxicity, thermal and chemical stability, high activity, antimicrobial potential, prolonged stability under light irradiation, etc. [15–18]. Furthermore, they present excellent electrochemical properties such as good cycling performance and high reversible specific capacity [19]. In addition, properties as porosity, particle size and surface area can be tailored by processing. Consequently, they are being studied in various fields such as photocatalysis for pollutant remediation, anode material for Li-ion batteries, gas sensor, adsorbents, photocathodes and photoanodes for water splitting, and for the breakdown of alcohols, hydrocarbons, etc [10,16,17,20].

Regarding wastewater treatment, advanced oxidation processes (AOPs) have gained interest over the last decades [21]. During AOPs, hydroxyl radicals ($^{\bullet}OH$) and other oxidants species are in-situ generated. These oxidants are capable of degrading refractory organic compounds. AOPs include ozonation [22], UV

radiation [23], Fenton/electro-Fenton processes [24] and electro-oxidation [25]. In the latter two techniques, the electrode material is considered an important factor in generating the •OH radicals [26,27]. Although ferrites have been used in different Fenton type processes for contaminant elimination [15,28], their application as a combined photo-anode for pollutant removal, which is the focus of this work, has not been widely studied.

Simultaneous photocatalytic (using visible light) and electrocatalytic oxidation of refractory organic contaminants in wastewaters is attracting attention, because it could combine photocatalysis using a large part of the solar spectrum and direct contact between photocatalytic active material and the substrate electrode to ensure rapid electron transport [29]. In addition, the need to separate the photocatalyst particles from wastewater, as is the case with Fenton processes, is avoided as they are attached on the electrode surface [30,31].

Some authors have deposited the photo-electrocatalysts over the conductive substrate by methods as sol-gel, electrodeposition, decomposition of a complex precursor, etc [32–37]. An option to simplify the deposition process is by dip-coating, where a suspension of small particles of the photocatalyst are fixed to the electrode surface by a thermal treatment. In previous works, Gilabert et al. used the solution combustion synthesis to create spinel ferrites as spongy powders with nanometric grain size very easy to micronize [38,39], which could be used in the dip-coating process.

In this work, the physical and photoelectrochemical characterization of two different ferrites has been studied, cadmium and calcium ferrites. These ferrites were synthesized over a ceramic substrate based on tin dioxide doped with antimony. This ceramic substrate has some advantages, such as low

manufacturing cost, good corrosion resistance and high oxygen overpotential, among others [27,40–45]. Once the electrodes were characterized, they were tested as photoanodes to degrade and mineralize an emerging contaminant, specifically atenolol (ATL). ATL is a pharmaceutical product belonging to the group of β-blockers which is used to treat several cardiovascular diseases [46]. The main drawback of its use is its low removal rate in conventional wastewater treatment plants [47]. However, this contaminant could be eliminated by other techniques, such as photoelectro-oxidation, and more specifically, using the ceramic electrode of this study [27,48,49].

2. Material and methods

The preparation of solutions and reagents is explained in the Supplementary Information.

2.1- Electrode fabrication

The processing conditions employed for the basic ceramic substrate (tin dioxide doped with antimony) were described in a previous work [50]. The ferrite precursors were synthesized by solution combustion synthesis (SCS) following a process previously used with spinel-type pigments [38,39]. Concretely, 15.42 g of cadmium nitrate tetrahydrate ($Cd(NO_3)_2 \cdot 4H_2O$) or 11,81 g of calcium nitrate tetrahydrate ($Ca(NO_3)_2 \cdot 4H_2O$), and 40.40 g of iron (III) nitrate nonahydrate ($Fe(NO_3)_3 \cdot 9H_2O$) were dissolved in 50 mL of distilled water in a magnetically stirred pyrex vessel. After complete dissolution of nitrates, 20.02 g of urea were added. The combustion process was carried out introducing the vessel in a furnace preheated at a temperature of 500 °C (BLF 1800, Carbolite Furnaces

Ltd) and holding it at that temperature for 20 min to favour the complete combustion reaction, before cooling. During soaking time, the sample dries, boils, foam, ignites and burns reaching temperature conditions of about 1500 °C [51]. After the synthesis, the dip-coating processes takes place which is fully explained in [49]. To estimate the interaction of the catalysts with the electrodes, a mixture of each catalyst with tin oxide was prepared (60/40 wt.%) and was thermally treated with the same cycle used to fix the catalyst over the electrode (room temperature to 1100 ºC at 25 $ºC \cdot min^{-1}$, 1 hour at 1100 ºC and cooling). The products were milled and characterized by XRD.

2.2- Electrode characterization

2.2.1- Physical characterization

For the physical characterization of the electrode, the bulk density and electrical resistivity parameters have been determined. In addition, diffractograms (before and after thermal treatment) and images of the electrode surface were obtained to analyse the distribution and composition of the catalyst particles. The equipment and methods used have already been explained in previous works [52].

As regards photoluminescence (PL) analysis, a confocal Raman microscope (Witec alpha300 R confocal Raman microscope, Ulm Germany) excited with a neon laser at 488 nm was used. These analyses were carried out for the basic and ferrites ceramic electrodes at room temperature.

2.2.2- Photoelectrochemical characterization

For the photoelectrochemical characterization of ferrites, a quartz reactor of 200 ml with a three-electrode configuration has been used (Fig. SM1(a) in Supplementary Information). The working electrode (anode) was the ferrite under study with a working area of 0.25 cm^2; while the counter electrode (cathode) was made of platinum (Pt) (Crison®, 52-67) and, close to the anodic surface, a silver/silver chloride (Ag/AgCl) reference electrode (Crison® 52 -40) encapsulated in a 3M potassium chloride (KCl) solution was employed. The three electrodes were connected to a potentiostat/galvanostat (AUTOLAB PGSTAT 302N) controlled with NOVA® software (Metrohm Autolab B.V.). The assays were carried out at room temperature in an electrolyte composed of 0.1 M sodium sulfate (Na_2SO_4). A 200 W Xenon lamp (Hamamatsu LC8) was used as a source of light, mainly in the visible spectrum. Moreover, an A9616–08 light filter was coupled to the lamp in order to avoid the infrared radiation.

Light pulse chronoamperometry was carried out at two different anodic potentials under intermittent light radiation with a pulse duration of 150 seconds. These potentials were selected by a previous linear sweep voltammetry (LSV) scan. LSV consisted of a potentiodynamic potential sweep at a scan rate of 50 $mV \cdot s^{-1}$ from the open circuit potential (OCP) to an overpotential of +2 Volts, in anodic direction. These assays were performed with and without illumination.

Band gap energy (E_g) is also an important parameter in the characterization of photoanodes [53,54]. This energy is calculated as the difference between the HOMO level (valence band) and LUMO level (conduction band) of the semiconductor materials. According to the literature [55,56], the E_g can be calculated by two methods: UV-Vis NIR spectroscopy and cyclic voltammetry

tests (CV). The first method is the most used, but it is an expensive method which requires a complex equipment [57,58], this is why the CV method was the selected option for this work. In this case, it is assumed that during the oxidation process a hole is incorporated in the HOMO level, while an electron is introduced in the LUMO level in the reduction one. These energy levels were calculated using the following equations:

$$E_{LUMO}(V\ vs\ SHE) = -(E_{red}(V\ vs\ Ag/AgCl) + 0.197 + 4.4) \quad (1)$$

$$E_{HOMO}(V\ vs\ SHE) = -(E_{ox}(V\ vs\ Ag/AgCl) + 0.197 + 4.4) \quad (2)$$

$$E_g(eV) = E_{LUMO} - E_{HOMO} = -E_{red} + E_{ox} \quad (3)$$

where E_{ox} and E_{red} are the onset oxidation and reduction potentials, respectively; +0.197 V is the conversion factor from the Ag/AgCl (saturated KCl) potential to the standard hydrogen electrode (SHE); and +4.4 V is the SHE energy level, reported with respect to the vacuum level. CV tests were carried out from the open circuit potential (OCP) towards positive potentials at a scan rate of 10 $mV \cdot s^{-1}$ until observing the E_{ox} of each ferrite. Afterwards, the potential scan was reversed in the cathodic direction until the E_{red} was observed. Finally, the potential sweep was again reversed to the OCP in the anodic direction.

2.3- Photoelectrolysis experiments

The reactor employed was the same as that used in the photoelectrochemical characterization experiments, filled with a 100 ppm of ATL (purity 98%, Sigma-Aldrich) in 2 $g \cdot L^{-1}$ of Na_2SO_4 (purity 99%, Panreac) solution. In these experiments (Fig. SM1(b) in Supplementary Information), the cathode was a 20 cm^2 stainless

198 steel sheet (AISI 304); the reference was an Ag/AgCl saturated in KCl electrode,
199 and as an anode, the above-mentioned calcium or cadmium ferrites were used,
200 which were immersed in the solution to obtain a contact surface area of 12 cm^2.
201 The distance between the cathode and anode electrodes was fixed at 2 cm. Two
202 different current densities values (16.67 and 66.67 $mA \cdot cm^{-2}$), supplied by a power
203 supply, were applied under light and darkness conditions. All tests were carried
204 out at a controlled temperature of 30 °C for 4 hours and under stirring conditions.
205 Electrode potential and cell voltage were recorded during the electrolysis. During
206 the first hour of electrolysis, samples were taken from the reactor every 15
207 minutes, and every 30 minutes thereafter. The lamp used was the same as that
208 employed in the previous section, but in this case a double beam was used to
209 illuminate the entire area of the anode.

210 The decay of the ATL concentration was controlled by measuring the extracted
211 samples using a high-performance liquid chromatograph (HPLC). The
212 mineralization of the contaminant was calculated with the measurement of total
213 organic carbon (TOC). Details of the HPLC and TOC methods are in
214 Supplementary Information.

215 Finally, the performance of mineralization was evaluated in terms of the
216 mineralization current efficiency (MCE, %) and the energy consumption per unit
217 of TOC depleted (E_{TOC}, kWh g_{TOC}^{-1}), for a given electrolysis time. These
218 parameters were calculated according to the following equations (4 and 5),
219 respectively [48,49]:

220

221 $$MCE(\%) = \frac{nFV\Delta(TOC)_t}{7.2 \cdot 10^5 mIt} \cdot 100 \quad (4)$$

$$E_{TOC} = \frac{\int_0^t U(t) \cdot I \, dt}{\Delta(TOC)_t \cdot V} \quad (5)$$

where the $\Delta[TOC]_t$ (mg·L^{-1}) is the difference in TOC concentration between the initial time and the value at given time *t* of electrolysis, *V* is the volume of electrolyte (L), *F* means the Faraday constant (96485 C·mol^{-1}), *m* is the number of carbon atoms in the ATL molecule ($C_{14}H_{22}N_2O_3$ which is 14 atoms), *I* is the applied current (A), the constant 7.2·10^5 is a conversion factor (=60 s·min^{-1} ·12000 mg C·mol^{-1}), *U* is the cell voltage (V) and *n* is theorical number electrons involved in the complete mineralization reaction of ATL (Equation 6)[48,59].

$$C_{14}H_{22}N_2O_3 + 25H_20 \rightarrow 14CO_2 + 2NH_4^+ + 64H^+ + 66e^- \quad (6)$$

It is worth noting that the E_{TOC} parameter does not consider the energy consumed by the lamp.

3. Results and discussion

3.1- Physical characterization of the electrode

The formation of the solid solution between the tin and antimony oxides caused the basic ceramic electrode to show a bluish colour (Fig. SM2 (a) in Supplementary Information). Their low bulk density (3657±14 kg·m^{-3}) allows estimating a porosity of around 47% by comparison with the true density of tin oxide. The mean resistivity of the specimens was 0.0222±0.0007 Ω·cm, sufficiently low to operate as an electrode, considering their ceramic nature.

245 The SCS process generates a reddish solid for the two precursors (Fig. SM2 (b)
246 and (c) in Supplementary Material), which were easy to disaggregate. XRD
247 characterisation (Fig. 1a) indicated that the precursor of cadmium ferrite (catalyst
248 A) consisted of a mixture of hematite (Fe_2O_3, rhombohedral, JCPDS file 01-079-
249 1741), monteponite (CdO, cubic, JCPDS file 00-005-0640) and a phase whose
250 diffractogram was like the cadmium hydroxide one (hexagonal, JCPDS file 01-
251 073-0969), but probably also contains some iron. On the other hand, the
252 precursor of calcium ferrite (catalyst B) includes hematite (Fe_2O_3, rhombohedral,
253 JCPDS file 00-033-0664), and a phase identified as double hydroxide of calcium
254 and iron ($Ca_3Fe_2(OH)_{12}$, cubic, JCPDS file 00-032-0166). This result points that
255 the SCS method does not allow the direct synthesis of the objective ferrites. In
256 addition, the crystallinity of the catalysts was low, a consequence of the fast
257 kinetics of the process.

258 The estimation of the final catalysts deposited over the electrode through the
259 phase composition of the calcined mixture of SnO_2 and each catalyst precursor
260 showed that the objective ferrites could be obtained. The product of the reaction
261 between catalyst A and tin oxide contained cassiterite (SnO_2, tetragonal JCPDS
262 file 00-041-1445), cadmium ferrite ($CdFe_2O_4$, cubic, JCPDS file 00-022-1063)
263 and a minor proportion of hematite (Fe_2O_3, rhombohedral, JCPDS file 01-073-
264 0603). In the case of the product of the reaction between catalyst B and tin oxide,
265 in addition to cassiterite, calcium ferrite ($CaFe_2O_4$, orthorhombic, JCPDS file 01-
266 072-1199), hematite (Fe_2O_3, rhombohedral, JCPDS file 01-089-0597), calcium
267 stannate ($CaSnO_3$, orthorhombic, JCPDS file 00-0310312) and calcium and iron
268 stannate ($Ca_{0,75}Fe_{1,5}Sh_{0,5}O_4$, orthorhombic, JCPDS file 01-084-1674) were
269 present (Fig. 1b). No mixed phases with tin oxide and iron or cadmium were

present, indicating that the reactivity between the catalyst A and the electrode was very low. In the case of catalyst B, its reactivity with the tin oxide was higher, but as a certain amount of the target phase was obtained, its photoelectrochemical behaviour was tested. In a previous work [60], during the manufacturing process of another ceramic ferrite ($BiFeO_3$), the authors observed that the desired product was not achieved, since it consisted of a mixture of two ferrites ($BiFeO_3$ and $Bi_2Fe_4O_9$).

Given that the thermal cycle designed to fix the catalyst over the electrode was nearly the same that the cycle used to test the reactivity of the catalysts with tin oxide (the only difference was a slower heating rate to oxidise the organic fluid), it can be assumed that a similar phase composition was obtained during such a treatment, but the proportion of phases containing tin was presumably lower as the contact catalyst-electrode was less intimate than in a powdered mixture.

The deposition of the catalyst over the electrode was not completely homogeneous as optical images demonstrates (Fig. SM3 in Supplementary Material). Furthermore, the individual particles did not lose their definition after the heat treatment, as shown in Fig. 2. The images also indicated that the particle size of the catalysts was mostly around one micron, as expected. However, catalyst A seemed to sinter in larger degree than catalyst B as the necks between the particles were more developed. It is probable that the higher phase purity expected in catalyst A favours their sintering with respect to catalyst B that presumably contains a mixture of some phases. In both cases the deposited layer was very porous and could favour the electrochemical reactivity of the catalysts. The EDX analysis of the electrode surfaces superimposed the signals of the tin oxide substrate with the signals of the elements present in each catalyst (Fig. 3).

295 Calcium and iron were detected in the electrode covered with catalyst A while
296 cadmium and iron were identified over the electrode covered with catalyst B.
297 These results confirm that the expected catalysts were present in the surface of
298 the electrodes.

299 The PL spectra obtained for both ferrites and the basic ceramic electrode are
300 shown in Fig. 4. It can be observed that when the basic ceramic electrode (Sb-
301 doped SnO_2) was irradiated with a 488 nm laser it did not emit
302 photoluminescence. However, ceramic ferrites showed an emission spectrum
303 with a broadband (between 550 and 940 nm, i.e. orange-red zone of the visible
304 and near infrared spectrum). For both ferrites, this broadband could be divided
305 into three bands: two centred bands on the red zone of the visible spectrum (at
306 700 and 750 nm) and another in the infrared zone at 840 nm. Other authors also
307 obtained similar spectra for different spinels excited at 488 nm [61,62].

308

309 *3.2- Photoelectrochemical characterization*

310 Fig. 5 shows linear sweep voltammograms obtained for the two ferrites, with and
311 without illumination. On the one hand, it can be observed that by irradiating visible
312 light on the cadmium ferrite, the resulting current density was greater than in the
313 darkness for potential values between 1 and 1.5 V vs Ag/AgCl and between 1.9
314 to 2.7 V vs Ag/AgCl; between the potential values of 1.5 and 1.9 V vs Ag/AgCl,
315 no differences were observed with and without light. On the other hand, with
316 calcium ferrite, according to the LSV the influence of light was notable from 2 V
317 to 3.1 V vs Ag/AgCl. Therefore, from these graphs, potential values of 1.7 and

2.1 V vs Ag/AgCl were selected to perform the light pulse chronoamperometries (Fig. 6).

As can be seen in Fig. 6, the smallest response to light was obtained at 1.7 V vs Ag/AgCl for both ferrites, as expected. For this potential value, calcium ferrite presented more influence of the visible radiation than cadmium ferrite. However, for the highest applied potential value (2.1 V vs Ag/AgCl), the anode most sensitive to illumination was the cadmium ferrite one. This trend agreed with LSVs shown in Fig. 5, since higher current densities of 2.1 V vs Ag/AgCl were reached for cadmium ferrite. These results corroborate the photoactivity of the ferrite photoanodes, as demonstrated by the authors in a previous study with another ferrite [60].

The cyclic voltammograms obtained for both anode materials are shown in Fig. 7. In the case of calcium ferrite, it was necessary to reach quite negative applied currents in order to observe E_{red}, therefore, the hysteresis phenomenon obtained in the curve was higher.

As can be seen in the Fig. 7, the onset oxidation potentials (E_{ox}) for cadmium and calcium ferrites were 2.4 and 2.07 V vs Ag/AgCl, respectively; and the onset reduction potentials were 1.1 and -0.57 V vs Ag/AgCl, respectively. Therefore, according to equations 1 to 3, the band gap energies obtained were 1.3 and 2.64 eV for Cd and Ca ferrites, respectively. These results indicate that both ferrites are a good option to be used as photoanodes, since their band gap energies (E_g) are higher than the dissociation value of water (1.23 eV) and are smaller than 3 eV which enhance solar absorption [53,63].

Comparing the E_g values obtained with previous studies, other authors [64] obtained similar band gap energy values for calcium ferrite (2.81 eV). However, for cadmium ferrites there is a wide range of values reported, from 0.65 to 2.05 eV [65,66]. Nevertheless, in these studies, it was shown that a higher manufacturing temperature results in lower values of E_g. In this work the temperature was 1100 °C, so, in future studies, it could be verified if synthetising this electrode at a lower temperature would increase the E_g value.

3.3- Photoelectrochemical performance

Once the phocatalytic activity of both ferrites was confirmed, experiments at different current densities, 16.67 and 66.67 $mA \cdot cm^{-2}$, were performed. Regarding the degradation of contaminant, for all the conditions studied, the ATL relative concentration decrease showed a pseudo-first order kinetic model related to an indirect oxidation process controlled by $^{\bullet}OH$ generation (Fig. SM4 in Supplementary Material). This behaviour was previously observed for the basic ceramic anodes (SnO_2 doped with Sb) without ferrite layers [48] and for Zn and Cd ferrites [49]. As can be seen in this figure, the ATL degradation was higher when the applied current density increased, as the concentration of $^{\bullet}OH$ increases with the applied current density [67]. Furthermore, ATL degradation was slightly faster under visible light irradiation for both applied current densities and ferrites, therefore its photocatalytic activity was verified. This behaviour was observed in previous studies with other ceramic ferrites [49,60]. As regards the pH evolution, the initial pH of the solution was around 7, and did not show much variation during all assays. As the pKa value of the ATL is 9.6 [48], the amino group of the molecule was protonated.

366 Table 1 presents the value of the apparent pseudo-first order kinetic constants
367 (k') obtained according to the proposed model. These results not only confirm the
368 improvement in the degradation rate of increasing the current density, but also
369 indicates that both ferrites use visible light to degrade ATL. Regarding the type of
370 ferrite, it can be observed that the cadmium ferrite electrode presented greater
371 degradation of ATL than the calcium one under both light and darkness
372 conditions. This could be related to its lower E_g value, since the number of
373 electrons reaching the conduction band from the valance band increases [65]. As
374 a result, the number of holes in the valence band also increases. This fact
375 benefits the formation of more $^{\bullet}OH$ free radicals. Another reason may be found
376 in the synthesis process, as it was mentioned above, it seems that the Cd ferrite
377 sintered better than the Ca one, since the necks between the particles were more
378 developed.

379 In a recent study, Rajeshwari et al. [68] obtained a k' value of 0.004 min^{-1} using
380 the visible light photo-Fenton technique with a $CuFe_2O_4/CdS/Bi_2S_3$ catalyst.
381 However, the k' values obtained in this previous work were lower than the values
382 obtained in present work, thus demonstrating that the visible light photoelectro-
383 oxidation technique with cadmium and calcium ferrites as anodes is a very
384 efficient technique.

385 Fig. 8 shows the evolution of the normalized TOC concentration against time for
386 the applied current densities under study under darkness and light conditions for
387 both ferrites. Regarding the mineralization of atenolol, for the same electrode,
388 when the applied current density increased and under light conditions, the
389 oxidation of the total organic matter was greater. In fact, it was observed that this
390 improvement under light conditions was more notable than that observed during

391 the degradation of the ATL. This could be explained by the fact that the
392 intermediates formed under these conditions were easier to oxidise. Moreover,
393 cadmium ferrite showed better results than calcium ferrite in terms of
394 mineralization, as observed previously in the degradation of ATL experiments.

395 For comparing the results obtained in the current work with those obtained in
396 other studies in which similar techniques have been used for ATL oxidation, a
397 comparative table has been prepared (Table SM1 in Supplementary Material).
398 The table shows the significant performance of cadmium and calcium ceramic
399 ferrites as photoanodes during ATL mineralization.

400 In regard to MCE (Fig. 9 (a) and (b)), for a given applied current density value
401 and same electrode, the use of visible light clearly enhanced MCE, although this
402 effect is higher for 16.67 $mA \cdot cm^{-2}$. This fact means that the irradiation on the
403 anode not only caused ATL degradation but also its mineralization as observed
404 previously. The effect on this parameter of the applied current density was the
405 opposite, that is, the MCE worsened with increasing applied current density, as
406 expected. This is because as the applied current density increases, secondary
407 reactions also increase, as observed in previous studies. [48,50]. Regarding the
408 type of ferrite, the resulting MCE values with cadmium ferrite were higher than
409 those obtained with calcium ferrite as the mineralization rate was higher. At 16.67
410 $mA \cdot cm^{-2}$, the mean MCE values for cadmium ferrite were 11.14% and 15.39% in
411 the absence and presence of visible light, respectively, and for calcium ferrite
412 were 4.82% and 10.55%, in the same conditions. For the highest applied current
413 density of 66.67 $mA \cdot cm^{-2}$, average MCE values of 3.72% and 4.75% were
414 obtained with cadmium ferrite in the absence and presence of visible light,
415 respectively, and with calcium ferrite a value of 3.66% was obtained for both

irradiation conditions. For all conditions, the MCE values obtained were low, but are typical values for these processes [48,49].

Finally, a similar effect was observed in terms of energy consumption (Fig. 9 (c) and (d)), where decreasing the applied current density and under light irradiation caused a decrease in E_{TOC}, specially for calcium ferrite. The effect of the applied current density on the figures of merit was the same as that observed for the bare ceramic anodes in previous works [48,49]. Therefore, the electrochemical oxidation process of the basic ceramic electrode (Sb-doped SnO_2) was improved by adding cadmium and calcium ferrites on the anode surface. Moreover, due to their photoactivity, the improvement was higher under sunlight, which is a clean, renewable and free energy.

4- Conclusions

In this work, two different ferrites (cadmium and calcium ferrites deposited on a Sb-doped SnO_2 ceramic surface) have been successfully synthesized to be used as photoanodes in photoelectrochemical oxidation processes of emerging contaminants. The purpose of this article was the physical and photoelectrochemical characterization of these new electrodes in order to employ them in the photoelectrochemical oxidation of atenolol.

From the physical characterization of each electrode, it was observed that in the thermal treatment the agglomerates of both particles were fixed, without losing their initial definition. Furthermore, it was observed that cadmium ferrites sintered

439 better than calcium ferrites, because the purity achieved was higher. For the
440 calcium ferrite, a mixture of some phases was observed.

441 From the photoelectrochemical characterization, both ferrites showed
442 photoactivity, especially for the potential of 2.1 V vs Ag/AgCl. Regarding the band
443 gap energy obtained, the value of cadmium ferrite (1.3 eV) was lower than that
444 obtained with calcium ferrite (2.64 eV). However, it was verified that both ferrites
445 were photoactive and a good option to be used as photoanodes, since their E_g
446 were greater than 1.23 eV and less than 3 eV. Concerning their use as
447 photoanodes, lower E_g value benefits the formation of $^{\bullet}OH$ free radicals, so the
448 effect of the manufacturing temperature on the E_g values could be evaluated in
449 future studies.

450 Photoelectrochemical assays showed that increasing the applied current
451 improves the ATL oxidation process, since an increase of more than 16% for the
452 degradation of ATL and 24% for its mineralization was achieved. Both parameters
453 were also enhanced under visible-light irradiation.

454 Comparing both ferrites, cadmium ferrite achieved better results in terms of the
455 photoelectrochemical oxidation process than cadmium ferrite, achieving values
456 of up to 96% ATL degradation compared to 91% with calcium ferrite and a
457 mineralization rate of 84.3% and 61.88%, respectively, at the same conditions.

458 Therefore, with these results, both ferrites are a good alternative in
459 photoelectrochemical oxidation processes of ATL, although cadmium ferrite
460 presents slightly better results in terms of degradation and mineralization than
461 calcium ferrite. In future work, its effectiveness as a photoanode for the
462 degradation of other emerging contaminants will be tested.

Acknowledgements

This work was supported by a Margarita Salas postdoctoral grant attributed to Julia Mora Gómez from Universitat Politècnica de València funded by Ministerio de Universidades, Plan de Recuperación, Transformación y Resilencia and the European Union-NextGeneration EU. In addition, this research has also been funded by the Conselleria d'Innovació, Universitats, Ciència i Societat Digital (Generalitat Valenciana, project reference: AICO/2021/128).

References

[1] A. Fujishima, K. Honda, Electrochemical Photolysis of Water at a Semiconductor Electrode, Nature. 238 (1972) 37–38. doi:https://doi.org/10.1038/238037a0.

[2] D. Chen, M. Sivakumar, A.K. Ray, Heterogeneous photocatalysis in environmental remediation, Dev. Chem. Eng. Miner. Process. 8 (2000) 505–550. doi:10.1002/apj.5500080507.

[3] D. Bahnemann, Photocatalytic water treatment: solar energy applications, Sol. Energy. 77 (2004) 445–459. doi:10.1016/j.solener.2004.03.031.

[4] N.G. Yadav, L.S. Chaudhary, P.A. Sakhare, T.D. Dongale, P.S. Patil, A.D. Sheikh, Impact of collected sunlight on $ZnFe_2O_4$ nanoparticles for photocatalytic application, J. Colloid Interface Sci. 527 (2018) 289–297. doi:10.1016/J.JCIS.2018.05.051.

[5] A. Fujishima, X. Zhang, D.A. Tryk, Heterogeneous photocatalysis: From

water photolysis to applications in environmental cleanup, Int. J. Hydrogen Energy. 32 (2007) 2664–2672. doi:10.1016/J.IJHYDENE.2006.09.009.

[6] D. Chatterjee, S. Dasgupta, Visible light induced photocatalytic degradation of organic pollutants, J. Photochem. Photobiol. C Photochem. Rev. 6 (2005) 186–205. doi:10.1016/j.jphotochemrev.2005.09.001.

[7] X. Yuan, D. Floresyona, P.H. Aubert, T.T. Bui, S. Remita, S. Ghosh, F. Brisset, F. Goubard, H. Remita, Photocatalytic degradation of organic pollutant with polypyrrole nanostructures under UV and visible light, Appl. Catal. B Environ. 242 (2019) 284–292. doi:10.1016/j.apcatb.2018.10.002.

[8] A. Arimi, L. Megatif, L.I. Granone, R. Dillert, D.W. Bahnemann, Visible-light photocatalytic activity of zinc ferrites, J. Photochem. Photobiol. A Chem. 366 (2018) 118–126. doi:10.1016/J.JPHOTOCHEM.2018.03.014.

[9] A. Šutka, R. Pärna, J. Kleperis, T. Käämbre, I. Pavlovska, V. Korsaks, K. Malnieks, L. Grinberga, V. Kisand, Photocatalytic activity of non-stoichiometric $ZnFe_2O_4$ under visible light irradiation, Phys. Scr. 89 (2014) 044011. doi:10.1088/0031-8949/89/04/044011.

[10] J.H. Kim, H.E. Kim, J.H. Kim, J.S. Lee, Ferrites: emerging light absorbers for solar water splitting, J. Mater. Chem. A. 8 (2020) 9447–9482. doi:10.1039/d0ta01554g.

[11] C. Cheng, H. Wang, J. Zhao, Y. Wang, G. Zhao, Y. Zhang, X. Liu, Y. Wang, Advances in the application of metal oxide nanozymes in tumor detection and treatment, Colloids Surfaces B Biointerfaces. 235 (2024) 113767. doi:10.1016/j.colsurfb.2024.113767.

[12] Y. Wang, G. Zhao, H. Chi, S. Yang, Q. Niu, D. Wu, W. Cao, T. Li, H. Ma, Q. Wei, Self-Luminescent Lanthanide Metal-Organic Frameworks as Signal Probes in Electrochemiluminescence Immunoassay, J. Am. Chem. Soc. 143 (2021) 504–512. doi:10.1021/jacs.0c12449.

[13] Y. Wang, G. Zhao, G. Zhang, Y. Zhang, H. Wang, W. Cao, T. Li, Q. Wei, An electrochemical aptasensor based on gold-modified MoS_2/rGO nanocomposite and gold-palladium-modified Fe-MOFs for sensitive detection of lead ions, Sensors Actuators B Chem. 319 (2020). doi:10.1016/j.snb.2020.128313.

[14] K.K. Kefeni, B.B. Mamba, T.A.M. Msagati, Application of spinel ferrite nanoparticles in water and wastewater treatment: A review, Sep. Purif. Technol. 188 (2017) 399–422. doi:10.1016/J.SEPPUR.2017.07.015.

[15] P. Roonasi, A.Y. Nezhad, A comparative study of a series of ferrite nanoparticles as heterogeneous catalysts for phenol removal at neutral pH, Mater. Chem. Phys. 172 (2016) 143–149. doi:10.1016/J.MATCHEMPHYS.2016.01.054.

[16] M.I.A.A. Maksoud, G.S. El-Sayyad, A.H. Ashour, A.I. El-Batal, M.A. Elsayed, M. Gobara, A.M. El-Khawaga, E.K. Abdel-Khalek, M.M. El-Okr, Antibacterial, antibiofilm, and photocatalytic activities of metals-substituted spinel cobalt ferrite nanoparticles, Microb. Pathog. 127 (2019) 144–158. doi:10.1016/J.MICPATH.2018.11.045.

[17] M. Madhukara Naik, H.S. Bhojya Naik, G. Nagaraju, M. Vinuth, H. Raja Naika, K. Vinu, Green synthesis of zinc ferrite nanoparticles in Limonia acidissima juice: Characterization and their application as photocatalytic

534 and antibacterial activities, Microchem. J. 146 (2019) 1227–1235.
535 doi:10.1016/J.MICROC.2019.02.059.

536 [18] A. Behera, D. Kandi, S. Mansingh, S. Martha, K. Parida, Facile synthesis
537 of $ZnFe_2O_4$@RGO nanocomposites towards photocatalytic ciprofloxacin
538 degradation and H_2 energy production, J. Colloid Interface Sci. 556 (2019)
539 667–679. doi:10.1016/J.JCIS.2019.08.109.

540 [19] N. Matinise, K. Kaviyarasu, N. Mongwaketsi, S. Khamlich, L. Kotsedi, N.
541 Mayedwa, M. Maaza, Green synthesis of novel zinc iron oxide ($ZnFe_2O_4$)
542 nanocomposite via Moringa Oleifera natural extract for electrochemical
543 applications, Appl. Surf. Sci. 446 (2018) 66–73.
544 doi:10.1016/J.APSUSC.2018.02.187.

545 [20] S.B. Patil, H.S. Bhojya Naik, G. Nagaraju, R. Viswanath, S.K. Rashmi, M.
546 Vijay kumar, Sugarcane juice mediated eco-friendly synthesis of visible
547 light active zinc ferrite nanoparticles: Application to degradation of mixed
548 dyes and antibacterial activities, Mater. Chem. Phys. 212 (2018) 351–362.
549 doi:10.1016/J.MATCHEMPHYS.2018.03.038.

550 [21] A. Hassani, M. Malhotra, A. V. Karim, S. Krishnan, P. V. Nidheesh, Recent
551 progress on ultrasound-assisted electrochemical processes: A review on
552 mechanism, reactor strategies, and applications for wastewater treatment,
553 Environ. Res. 205 (2022) 112463. doi:10.1016/j.envres.2021.112463.

554 [22] W. Chen, X. Li, Z. Pan, S. Ma, L. Li, Synthesis of MnOx/SBA-15 for
555 Norfloxacin degradation by catalytic ozonation, Sep. Purif. Technol. 173
556 (2017) 99–104. doi:10.1016/j.seppur.2016.09.030.

557 [23] L.V. de Souza Santos, A.M. Meireles, L.C. Lange, Degradation of

antibiotics norfloxacin by Fenton, UV and UV/H_2O_2, J. Environ. Manage. 154 (2015) 8–12. doi:10.1016/j.jenvman.2015.02.021.

[24] A. Özcan, A. Atılır Özcan, Y. Demirci, Evaluation of mineralization kinetics and pathway of norfloxacin removal from water by electro-Fenton treatment, Chem. Eng. J. 304 (2016) 518–526. doi:10.1016/j.cej.2016.06.105.

[25] S. Garcia-Segura, J.D. Ocon, M.N. Chong, Electrochemical oxidation remediation of real wastewater effluents — A review, Process Saf. Environ. Prot. 113 (2018) 48–67. doi:10.1016/J.PSEP.2017.09.014.

[26] A. Ahmadi, M. Zarei, A. Hassani, M. Ebratkhahan, A. Olad, Facile synthesis of iron(II) doped carbonaceous aerogel as a three-dimensional cathode and its excellent performance in electro-Fenton degradation of ceftazidime from water solution, Sep. Purif. Technol. 278 (2021) 119559. doi:10.1016/j.seppur.2021.119559.

[27] J. Mora-Gómez, M. García-Gabaldón, E. Ortega, M.-J. Sánchez-Rivera, S. Mestre, V. Pérez-Herranz, Evaluation of new ceramic electrodes based on Sb-doped SnO_2 for the removal of emerging compounds present in wastewater, Ceram. Int. 44 (2018) 2216–2222. doi:10.1016/J.CERAMINT.2017.10.178.

[28] M. Kurian, D.S. Nair, Heterogeneous Fenton behavior of nano nickel zinc ferrite catalysts in the degradation of 4-chlorophenol from water under neutral conditions, J. Water Process Eng. 8 (2015) e37–e49. doi:10.1016/J.JWPE.2014.10.011.

[29] R. Yang, Y. Ji, J. Zhang, R. Zhang, F. Liu, Y. Chen, L. Liang, S. Han, X.

582 Yu, H. Liu, Efficiently degradation of polyacrylamide pollution using a full
583 spectrum Sn_3O_4 nanosheet/Ni foam heterostructure photoelectrocatalyst,
584 Catal. Today. 335 (2019) 520–526. doi:10.1016/J.CATTOD.2019.02.019.

585 [30] R. Daghrir, P. Drogui, D. Robert, Photoelectrocatalytic technologies for
586 environmental applications, J. Photochem. Photobiol. A Chem. 238 (2012)
587 41–52. doi:10.1016/J.JPHOTOCHEM.2012.04.009.

588 [31] Y. fan Su, G.B. Wang, D.T.F. Kuo, M. ling Chang, Y. hsin Shih,
589 Photoelectrocatalytic degradation of the antibiotic sulfamethoxazole using
590 TiO_2/Ti photoanode, Appl. Catal. B Environ. 186 (2016) 184–192.
591 doi:10.1016/J.APCATB.2016.01.003.

592 [32] S.S. Kumbhar, M.A. Mahadik, S.S. Shinde, K.Y. Rajpure, C.H. Bhosale,
593 Fabrication of $ZnFe_2O_4$ films and its application in photoelectrocatalytic
594 degradation of salicylic acid, J. Photochem. Photobiol. B Biol. 142 (2015)
595 118–123. doi:10.1016/J.JPHOTOBIOL.2014.12.002.

596 [33] X. Zhao, T. Xu, W. Yao, C. Zhang, Y. Zhu, Photoelectrocatalytic
597 degradation of 4-chlorophenol at Bi_2WO_6 nanoflake film electrode under
598 visible light irradiation, Appl. Catal. B Environ. 72 (2007) 92–97.
599 doi:10.1016/J.APCATB.2006.10.006.

600 [34] X. Zhao, Y. Zhu, Synergetic degradation of rhodamine B at a porous
601 $ZnWO_4$ film electrode by combined electro-oxidation and photocatalysis,
602 Environ. Sci. Technol. 40 (2006) 3367–3372. doi:10.1021/es052029e.

603 [35] T. Zeng, X. Yu, K.H. Ye, Z. Qiu, Y. Zhu, Y. Zhang, $BiPO_4$ film on ITO
604 substrates for photoelectrocatalytic degradation, Inorg. Chem. Commun.
605 58 (2015) 39–42. doi:10.1016/J.INOCHE.2015.04.027.

606 [36] Y. Zhang, Z. Yi, G. Wu, Q. Shen, Novel Y doped $BiVO_4$ thin film electrodes
607 for enhanced photoelectric and photocatalytic performance, J. Photochem.
608 Photobiol. A Chem. 327 (2016) 25–32.
609 doi:10.1016/J.JPHOTOCHEM.2016.05.004.

610 [37] X. Zhao, J. Qu, H. Liu, C. Hu, Photoelectrocatalytic degradation of triazine-
611 containing azo dyes at γ-Bi_2MoO_6 film electrode under visible light
612 irradiation (λ > 420 Nm), Environ. Sci. Technol. 41 (2007) 6802–6807.
613 doi:10.1021/es070598b.

614 [38] J. Gilabert, M.D. Palacios, M.J. Orts, S. Mestre, Solution combustion
615 synthesis of (Ni,Fe)Cr_2O_4 pigments: Effect of post-synthesis thermal
616 treatments, Ceram. Int. 43 (2017) 12789–12798.
617 doi:10.1016/J.CERAMINT.2017.06.168.

618 [39] J. Gilabert, M.D. Palacios, V. Sanz, S. Mestre, Solution combustion
619 synthesis of (Co,Ni)Cr_2O_4 pigments: Influence of initial solution
620 concentration, Ceram. Int. 43 (2017) 10032–10040.
621 doi:10.1016/J.CERAMINT.2017.05.019.

622 [40] C.A. Martínez-Huitle, M. Panizza, Electrochemical oxidation of organic
623 pollutants for wastewater treatment, Curr. Opin. Electrochem. 11 (2018)
624 62–71. doi:10.1016/J.COELEC.2018.07.010.

625 [41] I.D. Santos, S.B. Gabriel, J.C. Afonso, A.J.B. Dutra, Preparation and
626 characterization of Ti/SnO_2-Sb electrode by Pechini's method for phenol
627 oxidation, Mater. Res. 14 (2011) 408–416. doi:10.1590/S1516-
628 14392011005000054.

629 [42] S.-P. Tong, C.-A. Ma, H. Feng, A novel PbO_2 electrode preparation and its

application in organic degradation, Electrochim. Acta. 53 (2008) 3002–3006. doi:10.1016/j.electacta.2007.11.011.

[43] Y. Wang, C. Shen, M. Zhang, B.T. Zhang, Y.G. Yu, The electrochemical degradation of ciprofloxacin using a SnO_2-Sb/Ti anode: Influencing factors, reaction pathways and energy demand, Chem. Eng. J. 296 (2016) 79–89. doi:10.1016/J.CEJ.2016.03.093.

[44] G. Zhao, Y. Zhang, Y. Lei, L. V. Baoying, J. Gao, Y. Zhang, D. Li, Fabrication and electrochemical treatment application of a novel lead dioxide anode with superhydrophobic surfaces, high oxygen evolution potential, and oxidation capability, Environ. Sci. Technol. 44 (2010) 1754–1759. doi:10.1021/es902336d.

[45] J. Carrillo-Abad, J. Mora-Gómez, M. García-Gabaldón, S. Mestre, V. Pérez-Herranz, Comparison between an electrochemical reactor with and without membrane for the nor oxidation using novel ceramic electrodes, J. Environ. Manage. 268 (2020). doi:10.1016/j.jenvman.2020.110710.

[46] A.N. Arenhart Heberle, M. García-Gabaldón, E.M. Ortega, A.M. Bernardes, V. Pérez-Herranz, Study of the atenolol degradation using a Nb/BDD electrode in a filter-press reactor, Chemosphere. 236 (2019) 124318. doi:10.1016/J.CHEMOSPHERE.2019.07.049.

[47] M. Biel-Maeso, R.M. Baena-Nogueras, C. Corada-Fernández, P.A. Lara-Martín, Occurrence, distribution and environmental risk of pharmaceutically active compounds (PhACs) in coastal and ocean waters from the Gulf of Cadiz (SW Spain), Sci. Total Environ. 612 (2018) 649–659. doi:10.1016/j.scitotenv.2017.08.279.

[48] J. Mora-Gómez, M. García-Gabaldón, J. Carrillo-Abad, M.T. Montañés, S. Mestre, V. Pérez-Herranz, Influence of the reactor configuration and the supporting electrolyte concentration on the electrochemical oxidation of Atenolol using BDD and SnO_2 ceramic electrodes, Sep. Purif. Technol. 241 (2020) 116684. doi:10.1016/j.seppur.2020.116684.

[49] J. Carrillo-Abad, J. Mora-Gómez, M. García-Gabaldón, M.T. Montañés, S. Mestre, V. Pérez-Herranz, Enhanced Atenolol oxidation by ferrites photoanodes grown on ceramic SnO_2-Sb_2O_3 anodes, J. Alloys Compd. 908 (2022) 164629. doi:10.1016/J.JALLCOM.2022.164629.

[50] J. Mora-Gómez, E. Ortega, S. Mestre, V. Pérez-Herranz, M. García-Gabaldón, Electrochemical degradation of norfloxacin using BDD and new Sb-doped SnO_2 ceramic anodes in an electrochemical reactor in the presence and absence of a cation-exchange membrane, Sep. Purif. Technol. 208 (2019) 68–75. doi:10.1016/J.SEPPUR.2018.05.017.

[51] K.C. Patil, M.S. Hegde, T. Rattan, S.T. Aruna, Chemistry of nanocrystalline oxide materials: combustion synthesis, properties and applications, world scientific, 2008.

[52] C. Domingo-Torner, V. Pérez-Herranz, M.C. Martí-Calatayud, S. Mestre, M. García-Gabaldón, Comparison of two different ceramic electrodes based on Sb-SnO_2 coated with $BiFeO_3$ and Bi_2WO_6 for the photoelectrooxidation of an emerging pollutant, J. Environ. Chem. Eng. 11 (2023). doi:10.1016/j.jece.2023.110616.

[53] M. Radecka, M. Rekas, A. Trenczek-Zajac, K. Zakrzewska, Importance of the band gap energy and flat band potential for application of modified TiO_2

photoanodes in water photolysis, J. Power Sources. 181 (2008) 46–55. doi:10.1016/j.jpowsour.2007.10.082.

[54] M.P. Cuins, H. Zhong, Ќ.S.S. Lo, T. Mirkovic, Y. Li, Y. Ding, Y. Li, G.D. Scholes, Noninjection Gram-Scale Synthesis of Monidisperse Pyramidal $CuInS_2$ Nanocrystals and Theri Size-Dependent Properties, ACS Nano. 4 (2010) 5253–5262. doi:10.1021/nn1015538 ©.

[55] L. Leonat, G. Sbârcea, I.V. Braňzoi, Cyclic voltammetry for energy levels estimation of organic materials, UPB Sci. Bull. Ser. B Chem. Mater. Sci. 75 (2013) 111–118.

[56] M. Al-Ibrahim, H.K. Roth, M. Schrödner, A. Konkin, U. Zhokhavets, G. Gobsch, P. Scharff, S. Sensfuss, The influence of the optoelectronic properties of poly(3-alkylthiophenes) on the device parameters in flexible polymer solar cells, Org. Electron. 6 (2005) 65–77. doi:10.1016/j.orgel.2005.02.004.

[57] B.W. D'Andrade, S. Datta, S.R. Forrest, P. Djurovich, E. Polikarpov, M.E. Thompson, Relationship between the ionization and oxidation potentials of molecular organic semiconductors, Org. Electron. 6 (2005) 11–20. doi:10.1016/j.orgel.2005.01.002.

[58] P. Kalinauskas, E. Norkus, Z. Mockus, R. Giraitis, R. Juškėnas, Electrochemical and Photoelectrochemical Characterization of Cu_2SnSe_3 Thin Films Deposited on Mo/Glass Substrates , J. Electrochem. Soc. 166 (2019) H3107–H3111. doi:10.1149/2.0161905jes.

[59] I. Sirés, N. Oturan, M.A. Oturan, Electrochemical degradation of β-blockers. Studies on single and multicomponent synthetic aqueous

solutions, Water Res. 44 (2010) 3109–3120. doi:10.1016/j.watres.2010.03.005.

[60] C. Domingo-Torner, M. García-Gabaldón, M.C. Martí-Calatayud, S. Mestre, V. Pérez-Herranz, Norfloxacin mineralization under light exposure using Sb–SnO_2 ceramic anodes coated with $BiFeO_3$ photocatalyst, Chemosphere. 313 (2023). doi:10.1016/j.chemosphere.2022.137518.

[61] M.E. Sadat, M. Kaveh Baghbador, A.W. Dunn, H.P. Wagner, R.C. Ewing, J. Zhang, H. Xu, G.M. Pauletti, D.B. Mast, D. Shi, Photoluminescence and photothermal effect of Fe_3O_4 nanoparticles for medical imaging and therapy, Appl. Phys. Lett. 105 (2014). doi:10.1063/1.4895133.

[62] V. Singh, R.P.S. Chakradhar, J.L. Rao, D.K. Kim, Combustion synthesized $MgAl_2O_4$:Cr phosphors-An EPR and optical study, J. Lumin. 129 (2009) 130–134. doi:10.1016/j.jlumin.2008.08.011.

[63] Y. Ji, M. Yang, H. Dong, T. Hou, L. Wang, Y. Li, Two-dimensional germanium monochalcogenide photocatalyst for water splitting under ultraviolet, visible to near-infrared light, Nanoscale. 9 (2017) 8608–8615. doi:10.1039/c7nr00688h.

[64] S. Chaveanghong, T. Kobkeatthawin, J. Trakulmututa, T. Amornsakchai, P. Kajitvichyanukul, S.M. Smith, Photocatalytic removal of 2-chlorophenol from water by using waste eggshell-derived calcium ferrite, RSC Adv. 13 (2023) 17565–17574. doi:10.1039/d3ra01357j.

[65] G.S.Y. Kumar, Optical and photocatalytic properties of $CdFe_2O_4$ nanocatalysts: Potential application in water treatment under solar light irradiation, Arch. Appl. Sci. Res. 5 (2013) 42–51.

https://www.scholarsresearchlibrary.com/abstract/optical-and-photocatalytic-properties-of-cdfe2o4-nanocatalysts-potential-application-in-water-treatment-under-solar-ligh-855.html.

[66] M. Naseri, Optical and magnetic properties of monophasic cadmium ferrite ($CdFe_2O_4$) nanostructure prepared by thermal treatment method, J. Magn. Magn. Mater. 392 (2015) 107–113. doi:10.1016/j.jmmm.2015.05.026.

[67] C. Comninellis, G. Chen, Electrochemistry for the Environment, Springer, New York, 2010.

[68] M.R. Rajeshwari, A. Syed, A.H. Bahkali, A.M. Elgorban, M.K. Rahiman, R.S. Varma, S.S. Khan, Enhanced photo-Fenton assisted photocatalytic degradation of atenolol using a novel rGO embedded double Z-scheme nano-heterojunction: Mechanism, kinetics and toxicity studies, J. Ind. Eng. Chem. 115 (2022) 402–415. doi:10.1016/j.jiec.2022.08.024.

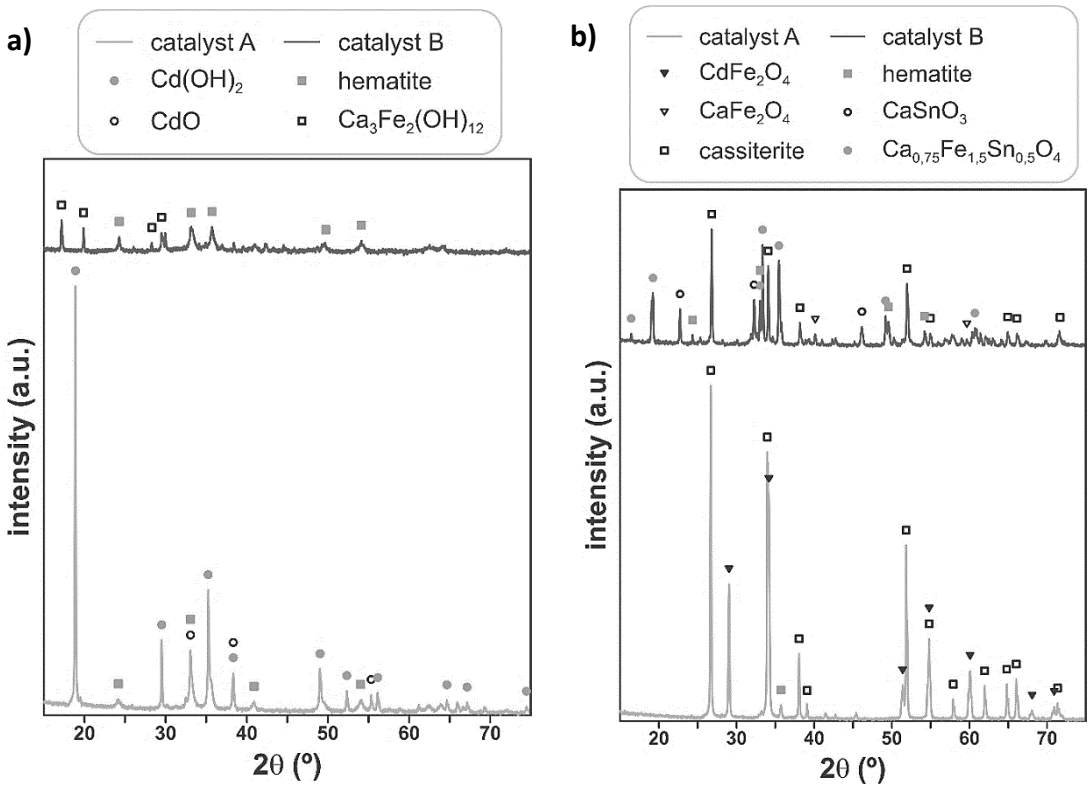

741 Fig. 1. Diffractograms of (a) the precursors of catalyst A (cadmium ferrite) and
742 catalyst B (calcium ferrite) synthesized by SCS before thermal treatment and (b)
743 the mixtures of tin oxide with the precursors of catalyst A and catalyst B after the
744 thermal treatment.

745

746

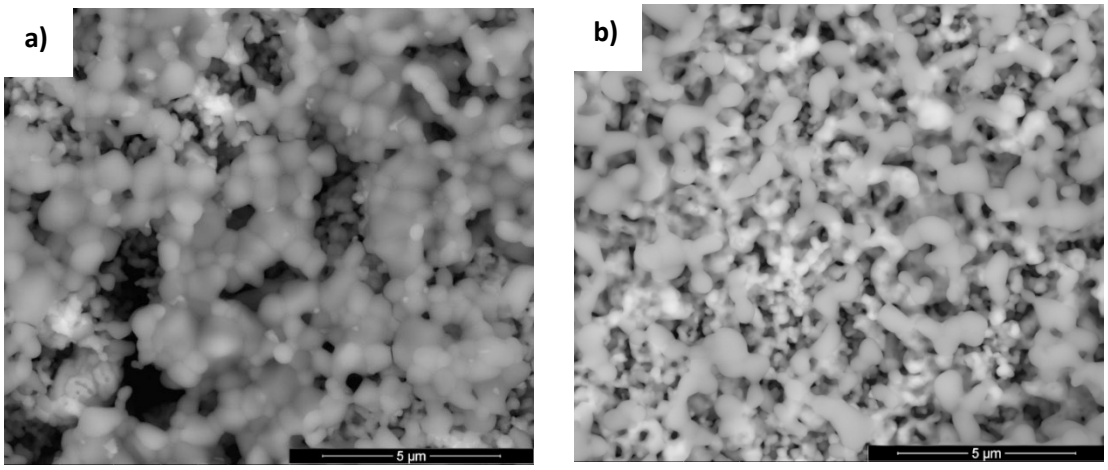

747 Fig. 2. SEM image of the electrode surface covered with (a) catalyst A and (b)

748 catalyst B.

749

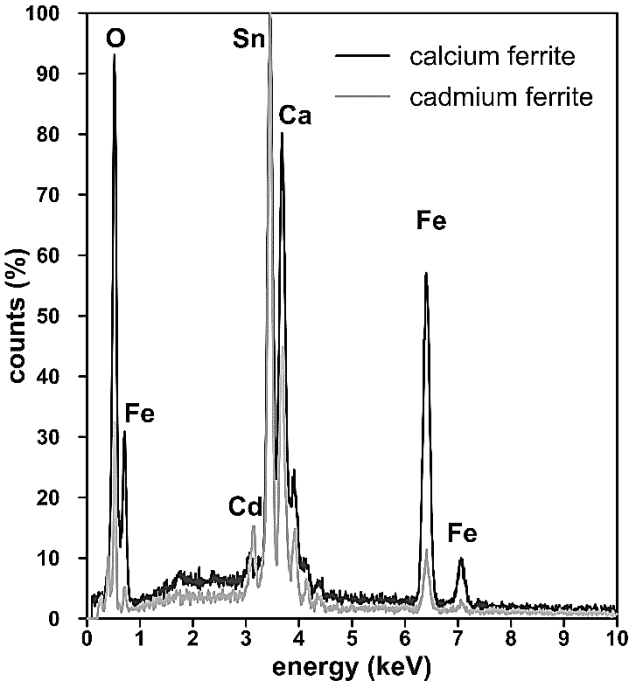

750

751 Fig. 3. EDX obtained of electrode surfaces covered with catalysts A and B.

752

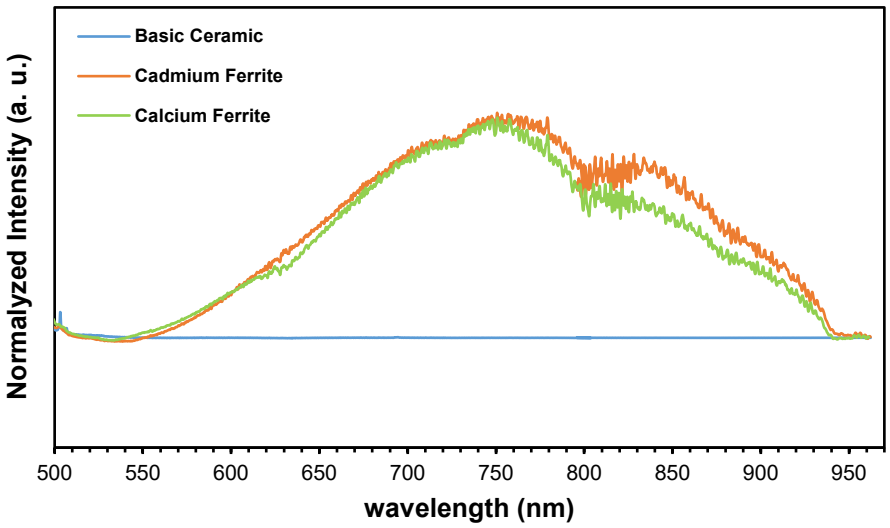

753

754 Fig. 4. PL spectra obtained with basic and ferrites ceramic electrodes (excited
755 with a neon laser at 488 nm).

756

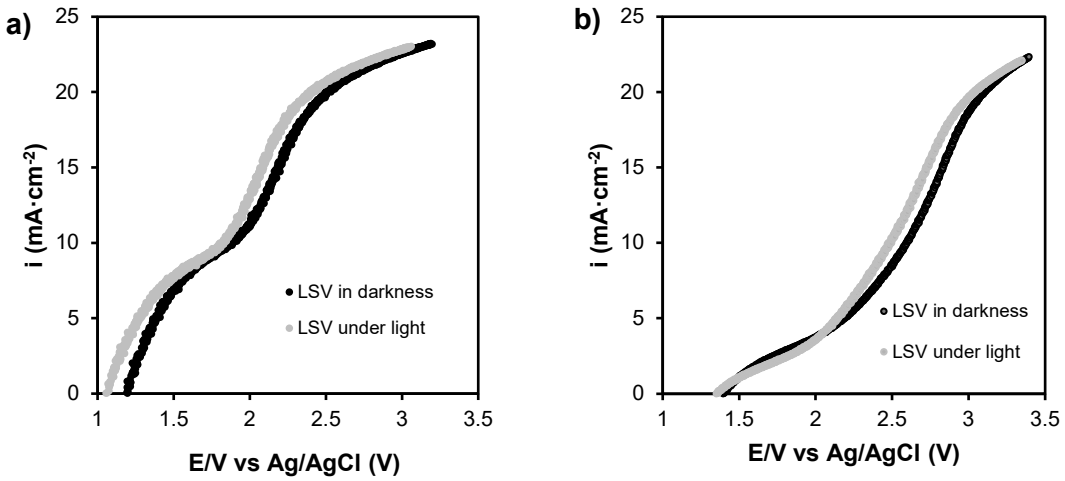

757 Fig. 5. LSV obtained for (a) cadmium and (b) calcium ferrites under light and
758 darkness conditions.

759

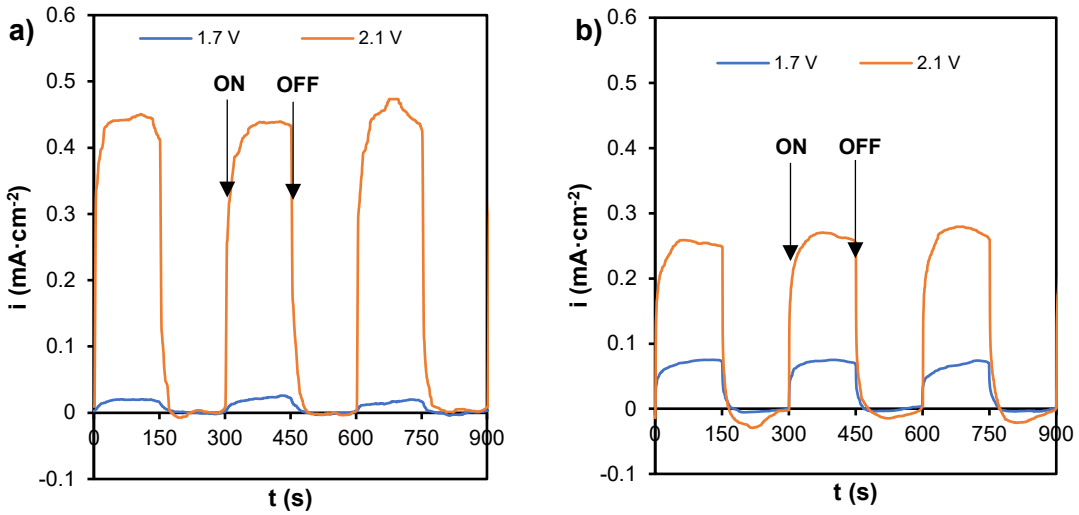

760 Fig. 6. Light pulses obtained at potentials of 1.7 and 2.1 vs Ag/AgCl with the (a)

761 cadmium and (b) calcium ferrites.

762

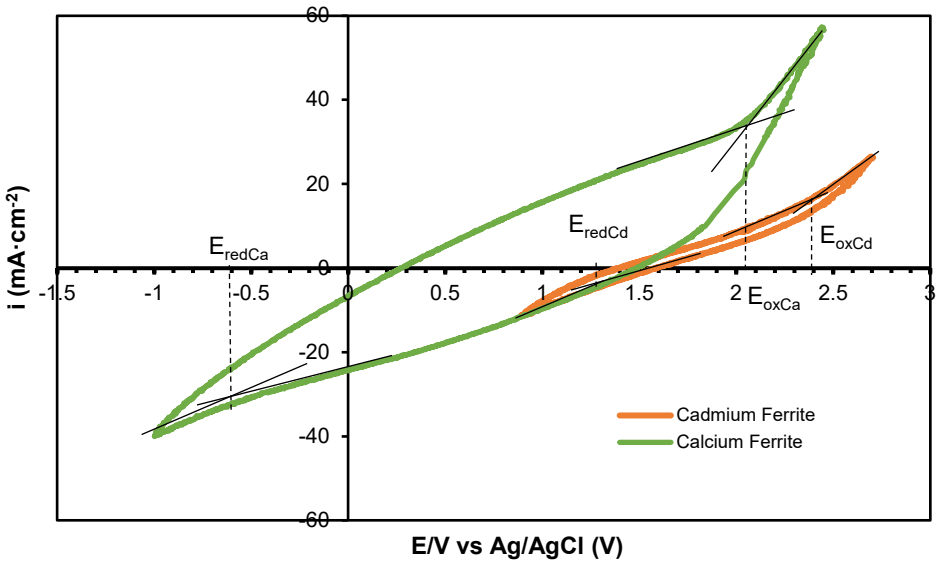

763

764 Fig. 7: Cyclic voltammetry curves obtained from both ferrites.

765

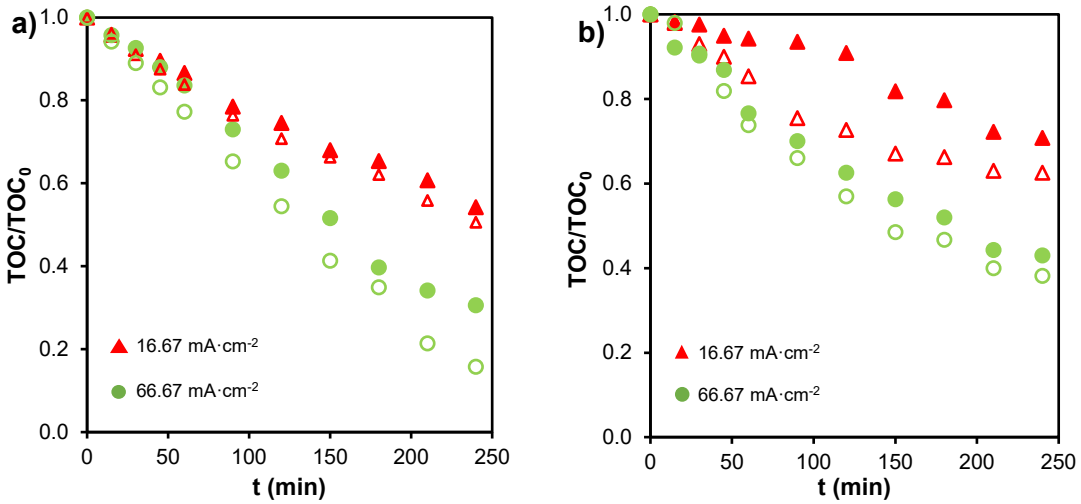

766 Fig. 8. Evolution of the normalized TOC concentration against time for the (a) Cd
767 ferrite and (b) Ca ferrite anodes under darkness (solid points) and light (empty
768 points) conditions for the applied current density values.

769

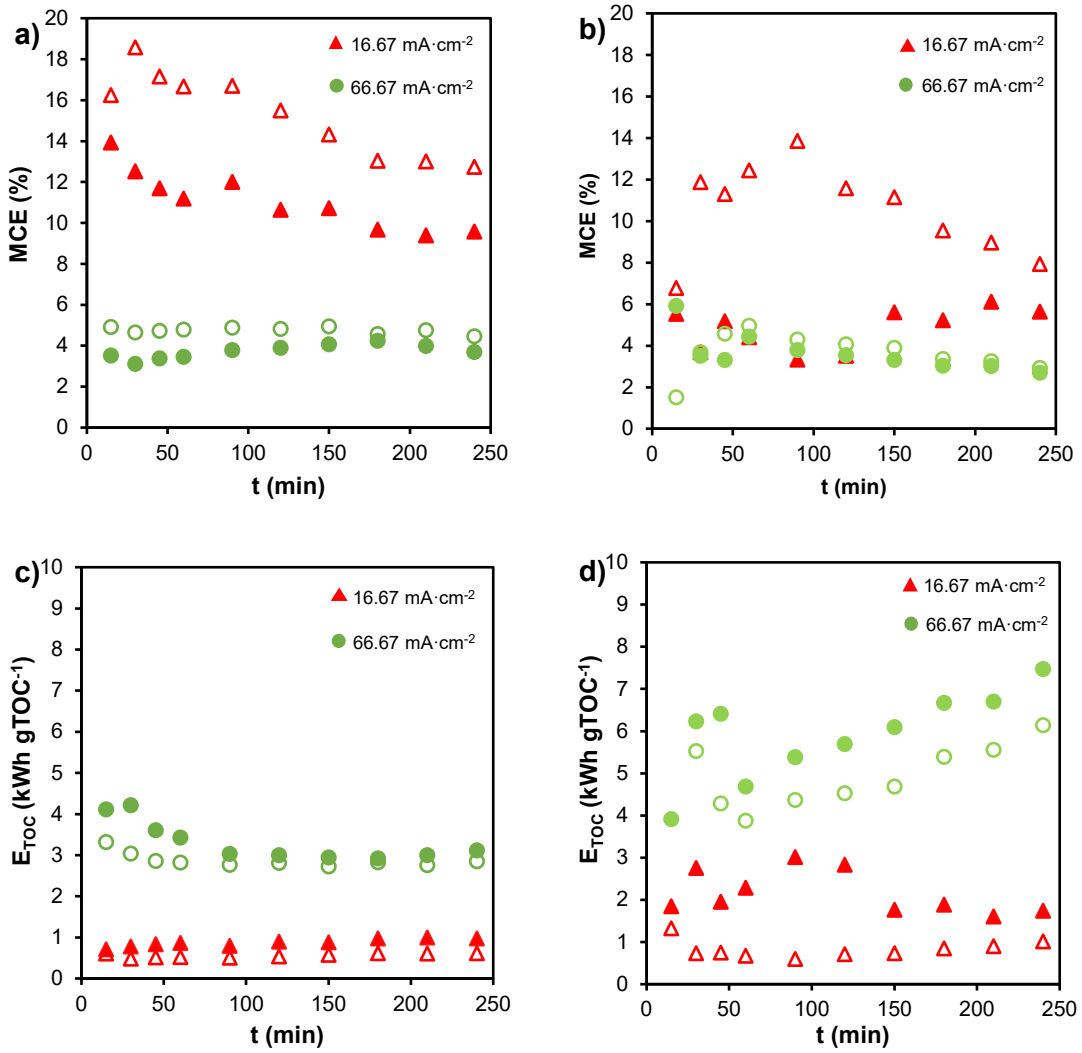

770 Fig. 9. Variation of the (a and b) MCE and (c and d) E_{TOC} with electrolysis time
771 for the (a and c) Cd ferrite and (b and d) Ca ferrite anodes under darkness (solid
772 points) and light (empty points) conditions for the applied current density values.

773

774

	Cadmium ferrite		Calcium ferrite	
i (mA·cm^{-2})	darkness	light	darkness	light
16.67	5.47	5.97	4.59	5.29
66.67	10.54	10.94	9.43	10.54

775 Table 1. Values of the pseudo first order rate constants (k′)·(10^{-3} min^{-1}) obtained

776 under darkness and light conditions for both ferrites.